Nonlinear polarization dynamics in a weakly birefringent all-normal dispersion photonic crystal fiber: toward a practical coherent fiber supercontinuum laser

Haohua Tu,[1,*] Yuan Liu,[1] Xiaomin Liu,[2] Dmitry Turchinovich,[2] Jesper Lægsgaard,[2] and Stephen A. Boppart[1]

[1]*Biophotonics Imaging Laboratory, Beckman Institute for Advanced Science and Technology, University of Illinois at Urbana-Champaign, Urbana, Illinois 61801, USA*

[2]*DTU Fotonik - Department of Photonics Engineering, Technical University of Denmark, DK-2800 Kgs. Lyngby, Denmark*

[*]*htu@illinois.edu*

Abstract: Dispersion-flattened dispersion-decreased all-normal dispersion (DFDD-ANDi) photonic crystal fibers have been identified as promising candidates for high-spectral-power coherent supercontinuum (SC) generation. However, the effects of the unintentional birefringence of the fibers on the SC generation have been ignored. This birefringence is widely present in nonlinear non-polarization maintaining fibers with a typical core size of 2 μm, presumably due to the structural symmetry breaks introduced in the fiber drawing process. We find that an intrinsic form-birefringence on the order of 10^{-5} profoundly affects the SC generation in a DFDD-ANDi photonic crystal fiber. Conventional simulations based on the scalar generalized nonlinear Schrödinger equation (GNLSE) fail to reproduce the prominent observed features of the SC generation in a short piece (9-cm) of this fiber. However, these features can be qualitatively or semi-quantitatively understood by the coupled GNLSE that takes into account the form-birefringence. The nonlinear polarization effects induced by the birefringence significantly distort the otherwise simple spectrotemporal field of the SC pulses. We therefore propose the fabrication of polarization-maintaining DFDD-ANDi fibers to avoid these adverse effects in pursuing a practical coherent fiber SC laser.

OCIS codes: (190.4370) Nonlinear optics, fibers; (320.6629) Supercontinuum generation; (060.2420) Fibers, polarization-maintaining; (060.5295) Photonic crystal fibers; (320.5520) Pulse compression.

References and links

1. P. Falk, M. Frosz, and O. Bang, "Supercontinuum generation in a photonic crystal fiber with two zero-dispersion wavelengths tapered to normal dispersion at all wavelengths," Opt. Express **13**(19), 7535–7540 (2005).
2. N. Nishizawa and J. Takayanagi, "Octave spanning high-quality supercontinuum generation in all-fiber system," J. Opt. Soc. Am. B **24**(8), 1786–1792 (2007).
3. A. M. Heidt, "Pulse preserving flat-top supercontinuum generation in all-normal dispersion photonic crystal fibers," J. Opt. Soc. Am. B **27**(3), 550–559 (2010).
4. H. Tu, Y. Liu, J. Lægsgaard, U. Sharma, M. Siegel, D. Kopf, and S. A. Boppart, "Scalar generalized nonlinear Schrödinger equation-quantified continuum generation in an all-normal dispersion photonic crystal fiber for broadband coherent optical sources," Opt. Express **18**(26), 27872–27884 (2010).
5. L. E. Hooper, P. J. Mosley, A. C. Muir, W. J. Wadsworth, and J. C. Knight, "Coherent supercontinuum generation in photonic crystal fiber with all-normal group velocity dispersion," Opt. Express **19**(6), 4902–4907 (2011).
6. H. Tu, Y. Liu, J. Lægsgaard, D. Turchinovich, M. Siegel, D. Kopf, H. Li, T. Gunaratne, and S. A. Boppart, "Cross-validation of theoretically quantified fiber continuum generation and absolute pulse measurement by MIIPS for a broadband coherently controlled optical source," Appl. Phys. B (2011), doi:10.1007/s00340-011-4746-2.

#156169 - $15.00 USD Received 7 Oct 2011; revised 16 Dec 2011; accepted 17 Dec 2011; published 4 Jan 2012

7. A. Hartung, A. M. Heidt, and H. Bartelt, "Design of all-normal dispersion microstructured optical fibers for pulse-preserving supercontinuum generation," Opt. Express **19**(8), 7742–7749 (2011).
8. Y. Silberberg, "Quantum coherent control for nonlinear spectroscopy and microscopy," Annu. Rev. Phys. Chem. **60**(1), 277–292 (2009).
9. D. L. Marks and S. A. Boppart, "Nonlinear interferometric vibrational imaging," Phys. Rev. Lett. **92**(12), 123905 (2004).
10. Th. Udem, R. Holzwarth, and T. W. Hänsch, "Optical frequency metrology," Nature **416**(6877), 233–237 (2002).
11. H. Tu and S. A. Boppart, "Optical frequency up-conversion by supercontinuum-free widely-tunable fiber-optic Cherenkov radiation," Opt. Express **17**(12), 9858–9872 (2009).
12. J. M. Dudley, G. Genty, and S. Coen, "Supercontinuum generation in photonic crystal fiber," Rev. Mod. Phys. **78**(4), 1135–1184 (2006).
13. F. Druon and P. Georges, "Pulse-compression down to 20 fs using a photonic crystal fiber seeded by a diode-pumped Yb:SYS laser at 1070 nm," Opt. Express **12**(15), 3383–3396 (2004).
14. B. von Vacano, T. Buckup, and M. Motzkus, "Shaper-assisted collinear SPIDER: fast and simple broadband pulse compression in nonlinear microscopy," J. Opt. Soc. Am. B **24**(5), 1091–1100 (2007).
15. B. Schenkel, R. Paschotta, and U. Keller, "Pulse compression with supercontinuum generation in microstructure fibers," J. Opt. Soc. Am. B **22**(3), 687–693 (2005).
16. T. Südmeyer, F. Brunner, E. Innerhofer, R. Paschotta, K. Furusawa, J. C. Baggett, T. M. Monro, D. J. Richardson, and U. Keller, "Nonlinear femtosecond pulse compression at high average power levels by use of a large-mode-area holey fiber," Opt. Lett. **28**(20), 1951–1953 (2003).
17. G. McConnell and E. Riis, "Ultra-short pulse compression using photonic crystal fibre," Appl. Phys. B **78**(5), 557–563 (2004).
18. A. M. Heidt, A. Hartung, G. W. Bosman, P. Krok, E. G. Rohwer, H. Schwoerer, and H. Bartelt, "Coherent octave spanning near-infrared and visible supercontinuum generation in all-normal dispersion photonic crystal fibers," Opt. Express **19**(4), 3775–3787 (2011).
19. A. Hartung, A. M. Heidt, and H. Bartelt, "Pulse-preserving broadband visible supercontinuum generation in all-normal dispersion tapered suspended-core optical fibers," Opt. Express **19**(13), 12275–12283 (2011).
20. G. Humbert, W. Wadsworth, S. Leon-Saval, J. Knight, T. Birks, P. St. J. Russell, M. Lederer, D. Kopf, K. Wiesauer, E. Breuer, and D. Stifter, "Supercontinuum generation system for optical coherence tomography based on tapered photonic crystal fibre," Opt. Express **14**(4), 1596–1603 (2006).
21. M.-L. V. Tse, P. Horak, F. Poletti, N. G. Broderick, J. H. Price, J. R. Hayes, and D. J. Richardson, "Supercontinuum generation at 1.06 mum in holey fibers with dispersion flattened profiles," Opt. Express **14**(10), 4445–4451 (2006).
22. Nonlinear Photonic Crystal Fiber NL-1050-NEG-1, *http://www.nktphotonics.com*
23. H. Wang, C. P. Fleming, and A. M. Rollins, "Ultrahigh-resolution optical coherence tomography at 1.15 mum using photonic crystal fiber with no zero-dispersion wavelengths," Opt. Express **15**(6), 3085–3092 (2007).
24. A. M. Heidt, J. Rothhardt, A. Hartung, H. Bartelt, E. G. Rohwer, J. Limpert, and A. Tünnermann, "High quality sub-two cycle pulses from compression of supercontinuum generated in all-normal dispersion photonic crystal fiber," Opt. Express **19**(15), 13873–13879 (2011).
25. J. K. Ranka, R. S. Windeler, and A. J. Stentz, "Visible continuum generation in air-silica microstructure optical fibers with anomalous dispersion at 800 nm," Opt. Lett. **25**(1), 25–27 (2000).
26. W. Q. Zhang, S. Afshar V, and T. M. Monro, "A genetic algorithm based approach to fiber design for high coherence and large bandwidth supercontinuum generation," Opt. Express **17**(21), 19311–19327 (2009).
27. D. Turchinovich, X. Liu, and J. Laegsgaard, "Monolithic all-PM femtosecond Yb-fiber laser stabilized with a narrow-band fiber Bragg grating and pulse-compressed in a hollow-core photonic crystal fiber," Opt. Express **16**(18), 14004–14014 (2008).
28. X. Liu, J. Laegsgaard, and D. Turchinovich, "Highly-stable monolithic femtosecond Yb-fiber laser system based on photonic crystal fibers," Opt. Express **18**(15), 15475–15483 (2010).
29. SuperK series supercontinuum lasers, *http://www.nktphotonics.com* SC series supercontinuum lasers, *http://www.fianium.com*
30. A. M. Weiner, D. E. Leaird, J. S. Patel, and J. R. Wullert II, "Programmable shaping of femtosecond optical pulses by use of 128-element liquid crystal phase modulator," IEEE J. Quantum Electron. **28**(4), 908–920 (1992).
31. A. M. Weiner, "Femtosecond pulse shaping using spatial light modulators," Rev. Sci. Instrum. **71**(5), 1929–1960 (2000).
32. D. Yelin, D. Meshulach, and Y. Silberberg, "Adaptive femtosecond pulse compression," Opt. Lett. **22**(23), 1793–1795 (1997).
33. W. J. Tomlinson, R. H. Stolen, and C. V. Shank, "Compression of optical pulses chirped by self-phase modulation in fibers," J. Opt. Soc. Am. B **1**(2), 139–149 (1984).
34. W. J. Tomlinson and W. H. Knox, "Limits of fiber-grating optical pulse compression," J. Opt. Soc. Am. B **4**(9), 1404–1411 (1987).
35. R. L. Fork, C. H. Cruz, P. C. Becker, and C. V. Shank, "Compression of optical pulses to six femtoseconds by using cubic phase compensation," Opt. Lett. **12**(7), 483–485 (1987).
36. M. Nisoli, S. De Silvestri, O. Svelto, R. Szipöcs, K. Ferencz, Ch. Spielmann, S. Sartania, and F. Krausz, "Compression of high-energy laser pulses below 5 fs," Opt. Lett. **22**(8), 522–524 (1997).
37. A. Baltuska, Z. Wei, M. S. Pshenichnikov, and D. A. Wiersma, "Optical pulse compression to 5 fs at a 1-MHz repetition rate," Opt. Lett. **22**(2), 102–104 (1997).

#156169 - $15.00 USD Received 7 Oct 2011; revised 16 Dec 2011; accepted 17 Dec 2011; published 4 Jan 2012

38. S. Lakó, J. Seres, P. Apai, J. Balázs, R. S. Windeler, and R. Szipőcs, "Pulse compression of nanojoule pulses in the visible using microstructure optical fiber and dispersion compensation," Appl. Phys. B **76**(3), 267–275 (2003).
39. Z. Várallyay, J. Fekete, Á. Bányász, and R. Szipőcs, "Optimizing input and output chirps up to the third-order for sub-nanojoule, ultra-short pulse compression in small core area PCF," Appl. Phys. B **86**(4), 567–572 (2007).
40. J. Thornes, P. Poon, and M. E. Anderson, "Single-iteration compression of femtosecond laser pulses," J. Opt. Soc. Am. B **21**(7), 1387–1390 (2004).
41. N. Karasawa, L. Li, A. Suguro, H. Shigekawa, R. Morita, and M. Yamashita, "Optical pulse compression to 5.0 fs by use of only a spatial light modulator for phase compensation," J. Opt. Soc. Am. B **18**(11), 1742–1746 (2001).
42. R. Trebino, *Frequency-Resolved Optical Gating: The Measurement of Ultrashort Laser Pulses* (Kluwer Academic, Dordrecht, 2002).
43. B. Schenkel, J. Biegert, U. Keller, C. Vozzi, M. Nisoli, G. Sansone, S. Stagira, S. De Silvestri, and O. Svelto, "Generation of 3.8-fs pulses from adaptive compression of a cascaded hollow fiber supercontinuum," Opt. Lett. **28**(20), 1987–1989 (2003).
44. K. Yamane, Z. Zhang, K. Oka, R. Morita, M. Yamashita, and A. Suguro, "Optical pulse compression to 3.4 fs in the monocycle region by feedback phase compensation," Opt. Lett. **28**(22), 2258–2260 (2003).
45. M. Adachi, K. Yamane, R. Morita, and M. Yamashita, "Sub-5-fs pulse compression of laser output using photonic crystal fiber with short zero-dispersion wavelength," Jpn. J. Appl. Phys. **44**(47), L1423–L1425 (2005).
46. E. Matsubara, K. Yamane, T. Sekikawa, and M. Yamashita, "Generation of 2.6 fs optical pulses using induced-phase modulation in a gas-filled hollow fiber," J. Opt. Soc. Am. B **24**(4), 985–989 (2007).
47. C. Iaconis and I. A. Walmsley, "Spectral phase interferometry for direct electric-field reconstruction of ultrashort optical pulses," Opt. Lett. **23**(10), 792–794 (1998).
48. H. Tu and S. A. Boppart, "Versatile photonic crystal fiber-enabled source for multi-modality biophotonic imaging beyond conventional multiphoton microscopy," Proc. SPIE **7569**, 75692CD (2010).
49. E. A. Golovchenko and A. N. Pilipetskii, "Unified analysis of four-photon mixing, modulational instability, and stimulated Raman scattering under various polarization conditions in fibers," J. Opt. Soc. Am. B **11**(1), 92–101 (1994).
50. S. Coen, A. Chau, R. Leonhardt, J. D. Harvey, J. C. Knight, W. J. Wadsworth, and P. St. J. Russell, "Supercontinuum generation by stimulated Raman scattering and parametric four-wave mixing in photonic crystal fibers," J. Opt. Soc. Am. B **19**(4), 753–764 (2002).
51. A. Apolonski, B. Povazay, A. Unterhuber, W. Drexler, W. J. Wadsworth, J. C. Knight, and P. St. J. Russell, "Spectral shaping of supercontinuum in a cobweb photonic-crystal fiber with sub-20-fs pulses," J. Opt. Soc. Am. B **19**(9), 2165–2170 (2002).
52. V. L. Kalashnikov, P. Dombi, T. Fuji, W. J. Wadsworth, J. C. Knight, P. St. J. Russell, R. S. Windeler, and A. Apolonski, "Maximization of supercontinua in photonic crystal bers by using double pulses and polarization effects," Appl. Phys. B **77**(2-3), 319–324 (2003).
53. Z. Zhu and T. Brown, "Experimental studies of polarization properties of supercontinua generated in a birefringent photonic crystal fiber," Opt. Express **12**(5), 791–796 (2004).
54. M. J. Steel, T. P. White, C. Martijn de Sterke, R. C. McPhedran, and L. C. Botten, "Symmetry and degeneracy in microstructured optical fibers," Opt. Lett. **26**(8), 488–490 (2001).
55. Z. Zhu and T. G. Brown, "Polarization properties of supercontinuum spectra generated in birefringent photonic crystal fibers," J. Opt. Soc. Am. B **21**(2), 249–257 (2004).
56. M. Tianprateep, J. Tada, and F. Kannari, "In uence of polarization and pulse shape of femtosecond initial laser pulses on spectral broadening in microstructure bers," Opt. Rev. **12**(3), 179–189 (2005).
57. G. P. Agrawal, *Nonlinear Fiber Optics*, 4th ed. (Academic Press, Boston, 2007).
58. M. Legré, M. Wegmuller, and N. Gisin, "Investigation of the ratio between phase and group birefringence in optical single-mode fibers," J. Lightwave Technol. **21**(12), 3374–3378 (2003).
59. G. Statkiewicz, T. Martynkien, and W. Urbanczyk, "Measurements of modal birefringence and polarimetric sensitivity of the birefringent holey fiber to hydrostatic pressure and strain," Opt. Commun. **241**(4-6), 339–348 (2004).
60. T. Ritari, H. Ludvigsen, M. Wegmuller, M. Legré, N. Gisin, J. Folkenberg, and M. Nielsen, "Experimental study of polarization properties of highly birefringent photonic crystal fibers," Opt. Express **12**(24), 5931–5939 (2004).
61. S. G. Murdoch, R. Leonhardt, and J. D. Harvey, "Polarization modulation instability in weakly birefringent fibers," Opt. Lett. **20**(8), 866–868 (1995).
62. B. Washburn, S. Ralph, and R. Windeler, "Ultrashort pulse propagation in air-silica microstructure fiber," Opt. Express **10**(13), 575–580 (2002).
63. D. V. Skryabin, F. Luan, J. C. Knight, and P. St. J. Russell, "Soliton self-frequency shift cancellation in photonic crystal fibers," Science **301**(5640), 1705–1708 (2003).
64. J. Dudley, X. Gu, L. Xu, M. Kimmel, E. Zeek, P. O'Shea, R. Trebino, St. Coen, and R. Windeler, "Cross-correlation frequency resolved optical gating analysis of broadband continuum generation in photonic crystal fiber: simulations and experiments," Opt. Express **10**(21), 1215–1221 (2002).
65. A. Efimov, A. Taylor, F. Omenetto, A. Yulin, N. Joly, F. Biancalana, D. Skryabin, J. Knight, and P. Russell, "Time-spectrally-resolved ultrafast nonlinear dynamics in small-core photonic crystal fibers: Experiment and modelling," Opt. Express **12**(26), 6498–6507 (2004).
66. K. L. Corwin, N. R. Newbury, J. M. Dudley, S. Coen, S. A. Diddams, K. Weber, and R. S. Windeler, "Fundamental noise limitations to supercontinuum generation in microstructure fiber," Phys. Rev. Lett. **90**(11), 113904 (2003).

#156169 - $15.00 USD Received 7 Oct 2011; revised 16 Dec 2011; accepted 17 Dec 2011; published 4 Jan 2012

67. D. R. Solli, C. Ropers, P. Koonath, and B. Jalali, "Optical rogue waves," Nature **450**(7172), 1054–1057 (2007).
68. F. Lu, Q. Lin, W. H. Knox, and G. P. Agrawal, "Vector soliton fission," Phys. Rev. Lett. **93**(18), 183901 (2004).
69. A. Michie, J. Canning, I. Bassett, J. Haywood, K. Digweed, M. Åslund, B. Ashton, M. Stevenson, J. Digweed, A. Lau, and D. Scandurra, "Spun elliptically birefringent photonic crystal fibre," Opt. Express **15**(4), 1811–1816 (2007).
70. A. Argyros, J. Pla, F. Ladouceur, and L. Poladian, "Circular and elliptical birefringence in spun microstructured optical fibres," Opt. Express **17**(18), 15983–15990 (2009).
71. C. Finot, B. Kibler, L. Provost, and S. Wabnitz, "Beneficial impact of wave-breaking for coherent continuum formation in normally dispersive nonlinear fibers," J. Opt. Soc. Am. B **25**(11), 1938–1948 (2008).
72. R. J. Kruhlak, G. K. Wong, J. S. Chen, S. G. Murdoch, R. Leonhardt, J. D. Harvey, N. Y. Joly, and J. C. Knight, "Polarization modulation instability in photonic crystal fibers," Opt. Lett. **31**(10), 1379–1381 (2006).
73. B. J. Chick, J. W. Chon, and M. Gu, "Polarization effects in a highly birefringent nonlinear photonic crystal fiber with two-zero dispersion wavelengths," Opt. Express **16**(24), 20099–20105 (2008).
74. M. Lehtonen, G. Genty, H. Ludvigsen, and M. Kaivola, "Supercontinuum generation in a highly birefringent microstructured □ber," Appl. Phys. Lett. **82**(14), 2197–2199 (2003).
75. A. Proulx, J.-M. Ménard, N. Hô, J. Laniel, R. Vallée, and C. Paré, "Intensity and polarization dependences of the supercontinuum generation in birefringent and highly nonlinear microstructured fibers," Opt. Express **11**(25), 3338–3345 (2003).
76. Z. Zhu and T. G. Brown, "Stress-induced birefringence in microstructured optical fibers," Opt. Lett. **28**(23), 2306–2308 (2003).

1. Coherent supercontinuum generation by all-normal dispersion photonic crystal fibers

Several recent studies have theoretically and experimentally identified the advantages of the dispersion-flattened dispersion-decreased all-normal dispersion (DFDD-ANDi) fibers for broadband coherent supercontinuum (SC) generation [1–6]. A typical DFDD-ANDi photonic crystal fiber (PCF) has a flattened convex profile of normal dispersion [Fig. 1(a)] [1, 3–5], whereas the wavelength at the convex point can be termed as the minimal dispersion ($|D|$ or β_2) wavelength (MDW). Just like the well-documented dispersion engineering that shifts the zero-dispersion-wavelength (ZDW) of a conventional PCF anywhere between 550 and 1250 nm [Fig. 1(b)], specific dispersion engineering can place the MDW of a DFDD-ANDi PCF anywhere inside this spectral region [Fig. 1(a)] [4, 7]. The interest in DFDD-ANDi PCFs is driven by the need of a practical fiber SC source with full coherence among all the frequency components of the SC. Broadband coherent sources are indispensible in coherent nonlinear microscopy [8, 9], frequency metrology [10], nonlinear frequency conversion/amplification, ultrashort pulse generation, and other coherently controlled applications.

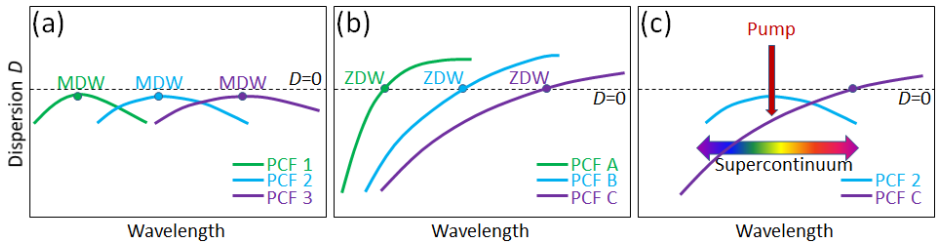

Fig. 1. (a) Dispersion engineering of DFDD-ANDi PCFs; (b) Dispersion engineering of ZDW PCFs; (c) Comparison of supercontinuum generation in a DFDD-ANDi PCF and a ZDW PCF.

For a pump laser emitting short (fs or ps) pulses at a given wavelength λ_p, it is nontrivial to select the optimal ZDW PCF for broadband coherent SC generation. The nonlinear frequency generation of a PCF having a ZDW of λ_{ZDW} can be broadly classified into three operating regimes: (1) $\lambda_{ZDW} << \lambda_p$, soliton-Cherenkov-radiation regime. In this regime the pump pulses transfer their energy into discrete bands of solitons and Cherenkov radiation(s), so that SC is not generated [11]. (2) $\lambda_{ZDW} \approx \lambda_p$, incoherent SC generation regime. This regime has generated the broadest SC via soliton excitation, and has received the most attention. The coherence of the SC is generally poor [12], but can be improved for pulse compression by (undesirably) decreasing the bandwidth and power spectral density of the generated SC [13, 14], or employing very short (5 mm) fiber lengths and short (15 fs) pump pulses [15]. (3) $\lambda_{ZDW} >> \lambda_p$, coherent SC generation regime. This regime produces relatively narrow bandwidth SC mainly

#156169 - $15.00 USD Received 7 Oct 2011; revised 16 Dec 2011; accepted 17 Dec 2011; published 4 Jan 2012

through self-phase modulation. However, the generated SC has full coherence [12], which has been demonstrated by pulse compression [16, 17].

On the other hand, it is relatively straightforward to select the optimal DFDD-ANDi PCF for broadband coherent SC generation by matching the MDW of the fiber with λ_p [Fig. 1(a)] [3–5]. The mismatch between the two leads to the increased dispersion $|D|$ at or near λ_p [Fig. 1(a)], which is unfavorable for nonlinear spectral broadening [18]. Because only the SC generation in a normal dispersion region of the fiber is guaranteed to be coherent, it is fair to compare the performance of the optimized DFDD-ANDi PCF with that of the ZDW PCF operated in the third regime ($\lambda_{ZDW} >> \lambda_p$) [Fig. 1(c)]. Due to the sloped dispersion profile of the ZDW PCF, the λ_{ZDW} of the fiber must be placed at a longer wavelength than the red edge of the intended SC. Thus, an undesirably large dispersion $|D|$ occurs at λ_p to adversely influence the spectral broadening [Fig. 1(c)]. This clearly illustrates the advantage of the DFDD-ANDi PCF over the conventional ZDW PCF in broadband coherent SC generation.

DFDD-ANDi PCFs have been fabricated in-house with a MDW around 625 nm [19], 800 nm [20], and 1050 nm [5, 21], while the SC generation from these fibers has exhibited excellent coherence. Also, a DFDD-ANDi PCF with a MDW of 1050 nm has been commercially available [22] and extensively studied [4, 6, 18, 23, 24]. This trend reflects newly-recognized PCF dispersion engineering [Fig. 1(a)] to preserve the coherence of the SC generation, as opposed to the well-known PCF dispersion engineering [Fig. 1(b)] to pursue the SC generation of the broadest bandwidth [25]. It is possible that the dispersion of typical DFDD-ANDi PCFs [4, 7] can be further flattened and decreased by intelligent fiber design (e.g., using genetic algorithm [26]). The combination of a DFDD-ANDi PCF having a MDW of ~1050 nm with an all-fiber ultrafast ytterbium laser oscillator [27, 28] could lead to a robust coherent fiber SC source with minimal (amplitude and phase) noise and acceptable bandwidth, which would nicely complement the widely used incoherent fiber SC sources [29]. Despite the progress along this line of research, the noticeable effect of the birefringence of the DFDD-ANDi PCFs on the SC generation [4, 23] has been completely ignored. Here we theoretically and experimentally demonstrate the profound effect of this birefringence in the commercial DFDD-ANDi PCF [22]. We recognize that the full advantages of the DFDD-ANDi PCFs for SC generation can be realized by intentionally introducing a strong linear birefringence to suppress any unintentional birefringence of random nature.

2. Enhanced noniterative pulse compression on theoretically-quantified supercontinuum

One sufficient condition and popular method to validate the coherent SC generation is to compress the SC pulses to the transform-limit. Until now, representative experimental studies on ultrashort (<35 fs) pulse compression of fiber SC have largely followed two distinct paths: (1) noniterative pulse compression by conventional pulse compressors (prisms, gratings, chirped mirrors) on theoretically-quantified SC; and (2) iterative (or adaptive) pulse compression by programmable pulse shaper [30, 31] on uncharacterized SC [32].

In the first path [Fig. 2(a)], the input SC pulses can be characterized by the scalar nonlinear Schrödinger equation (S-NLSE) [33, 34] to guide the pulse compression, while the compressed pulses are measured by an interferometric autocorrelator. This guidance allows simultaneous removal of the second- and third-order phase distortions, leading to sub-6 fs pulse compression [35–37]. However, the complicated pump lasers (low repetition rate amplifiers) have limited the widespread application of the corresponding sources. The same approach (except for some modifications to the S-NLSE [13, 38, 39]), when applied to the combination of a standard laser oscillator with a ZDW PCF, has not generated compressed pulses shorter than 12 fs [13, 16, 17, 38, 39]. The pulse width is limited by the coherent bandwidth of the SC, which has been limited to the short-wavelength side of the ZDW of the fiber [17, 38, 39], soliton fission [13], or large fiber dispersion at the pump wavelength [16]. We note that these limitations are no longer applicable to the DFDD-ANDi PCFs [Fig. 1(c)].

The conventional compressors employed in the first path are unable to compensate the higher-order phase distortions of the SC pulses, so that it is difficult to attain the transform-limited compression, i.e., to validate the full coherence of the SC. This key disadvantage is

#156169 - $15.00 USD Received 7 Oct 2011; revised 16 Dec 2011; accepted 17 Dec 2011; published 4 Jan 2012

directly addressed by the second path that typically employs a spatial light modulator (SLM)-based 4*f* pulse shaper for full phase compensation [Fig. 2(b)]. To circumvent the possible problematic calibration of the SLM [31, 40] and the possible difficulty to theoretically quantify the SC pulses, feedback control based on the measured spectral phase of the pulses from a dedicated pulse-temporal-field measurement device is employed. For this pulse measurement, an early study [41] used frequency resolved optical gating (FROG) [42], but later studies [14, 15, 43–46] universally adopted the spectral phase interferometry for direct electric-field reconstruction (SPIDER) [47]. For fully coherent SC pulses, one would expect this approach to achieve transmit-limited compression in all cases. However, the compressed pulses from most studies were far from the transform-limits, and due to the iterative nature of the feedback control, it is unclear whether this inability originated from the insufficient coherence of the SC pulses, the finite pixel number of the SLM, or the error from the pulse-temporal-field measurement device. Also, because the input SC pulses are not theoretically quantified, the selection of the fiber and the corresponding pump laser is more like art than science.

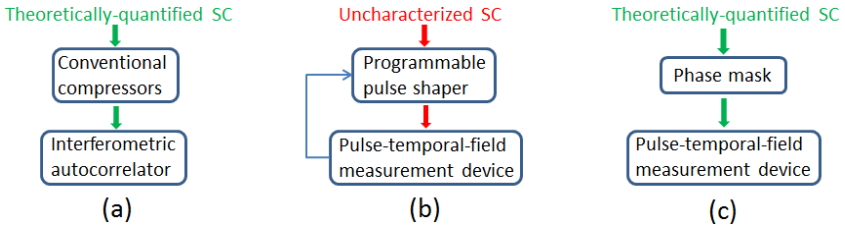

Fig. 2. Three representative paths for pulse compression of fiber supercontinuum.

The critical limitations of both paths can be prevented by taking a third path [Fig. 2(c)], termed as noniterative pulse compression by using a phase mask on theoretically-quantified SC. With the inclusion of the phase mask for full phase compensation, this path can be treated as an enhanced version of the first path. However, few (if not none) studies have taken this path until our two recent studies on a DFDD-ANDi PCF [4, 6], the main results of which are summarized in Fig. 3. Cross-validation was achieved between the measured spectrotemporal field (both the spectrum and the spectral phase) of the SC pulses by a pulse-temporal-field measurement device and the calculated field by scalar generalized nonlinear Schrödinger equation (S-GNLSE) [Fig. 3(a)]. Thus, a calibrated dispersion-free SLM (which functions as the phase mask) compensated the phase distortion of the pulses to generate the corresponding transform-limited pulses of 9.6-fs [Fig. 3(b)], and the full coherence of the SC was experimentally confirmed [6]. In comparison to the 229-fs 8-nm FWHM pump laser pulses [Fig. 3(a)] that generate the fiber continuum, the compressed pulses reflect a compression ratio of 24. These two studies clearly demonstrated the predictability and reliability to control the fiber SC generation with broad spectral broadening. To realize the pulse compression of a given SC along the third path, it is advantageous to employ deterministic SC generation processes free of soliton-induced noise [12], and to produce relatively smooth spectral phase [Fig. 3(a)] that can be accurately retrieved by the pulse-temporal-field measurement device. Both restrictions favor the SC generation by the DFDD-ANDi PCFs over that by the ZDW PCFs operated in the second regime [Fig. 1(b)].

Our experimental studies [4, 6] have largely followed the theoretical concepts of Heidt [3] to develop an oscillator-pumped coherent fiber SC laser with high spectral power and single-pulse temporal profile [Fig. 3(b)] [2, 3, 7, 18, 19]. Because of the similarity of the S-GNLSE-based simulation employed in these studies, one would expect that the beneficial features of broader bandwidth (750-1350 nm) and flatter (±1 dB) spectrum foreseen by Heidt be readily attained in long (>9 cm) fibers, while the pulse compressibility be retained. We and another independent team have indeed realized the foreseen broad bandwidth and spectral flatness [5, 48]. However, neither team has demonstrated the expected pulse compressibility. A third team also generated spectrally-smooth broadband coherent SC from a rather different DFDD-ANDi

#156169 - $15.00 USD Received 7 Oct 2011; revised 16 Dec 2011; accepted 17 Dec 2011; published 4 Jan 2012

fiber [2]. Through the S-GNLSE-based simulation, they claimed that the SC should be readily compressible, but have never carried out such pulse compression thereafter. This coincidence seems to suggest the limitation of the S-GNLSE in guiding the high-compression-ratio (>24) pulse compression of the SC from long fibers, despite its success in a short (9-cm) fiber (Fig. 3). In the following sections we use the simulation based on the coupled GNLSE (C-GNLSE) [49] to reveal the sensitivity of the SC generation to the weak birefringence of the commercial DFDD-ANDi PCF [22]. We then present experimental evidence to show how this factor limits the intended broadband pulse compression. Finally, we design a dedicated experiment and perform the corresponding C-GNLSE-based simulation to guide the design of a PCF that can circumvent this difficulty.

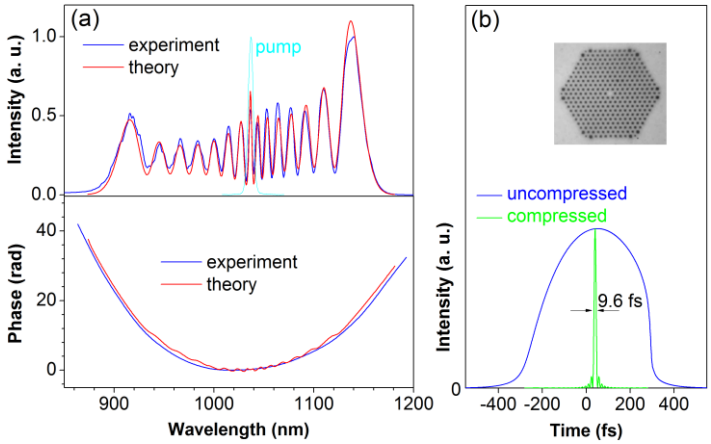

Fig. 3. (a) Comparison of measured spectrum and spectral phase of SC pulses with calculated spectrum and spectral phase from S-GNLSE. The spectrum of pump laser is also shown. (b) Temporal intensity profiles of uncompressed and compressed SC pulses. Inset: cross-section image of the DFDD-ANDi PCF.

3. Simulation by coupled generalized nonlinear Schrödinger equation (C-GNLSE)

3.1 Simulation of fiber supercontinuum generation: C-GNLSE vs. S-GNLSE

Independent experimental evidence has demonstrated the sensitive dependence of the SC generation on the polarization of the pump laser in a variety of ZDW PCFs with no intentional birefringence [50–53]. These fibers have a core area that is typical of SC-generating PCFs, and have a hexagonally (or pentagonally) symmetric cross-section which should make the fibers non-birefringent [54]. Thus, the observed polarization effects can only be attributed to the weak unintentional form-birefringence (B =1×10^{-6}-5×10^{-5}) intrinsic to these nonlinear fibers. Therefore, a complete understanding of the corresponding SC generation must rely on the C-GNLSE that takes account of this birefringence, rather than the S-GNLSE that ignores this effect. Ironically, the simulation of the SC generation in nonlinear PCFs has been largely restricted to the S-GNLSE [12], possibly because the physical insights gained from the C-GNLSE [50, 55, 56] are complicated by a wide selection of fibers and pump lasers [50–53], by the presence of noise [55], and by the random nature of the birefringence or uncontrolled fiber bending in long fibers [57].

We believe the SC generation in the 9-cm DFDD-ANDi PCF (Fig. 3) is an excellent case to reveal the underlying polarization effects. First, the measured spectrotemporal field and the calculated field by the S-GNLSE are in excellent agreement when the incident pump pulses are aligned along one of the principal axis of the fiber [Fig. 3(a)] [4]. This is a good starting point to investigate the effect of incident polarization with minimum ambiguity. Second, the SC is generated deterministically in a normal dispersion region of the fiber so that the noise can be ignored [3, 12]. Third, the simulation on relatively short fibers minimizes the

#156169 - $15.00 USD Received 7 Oct 2011; revised 16 Dec 2011; accepted 17 Dec 2011; published 4 Jan 2012

randomness of the birefringence and the uncontrolled fiber bending, enabling direct comparison with experiments.

3.2 Predicted polarization effects by C-GNLSE in a weakly birefringent DFDD-ANDi PCF

By ignoring the polarization dependence of the higher order dispersion coefficients (β_k, k>2) and the orthogonal component of the Raman susceptibility, the C-GNLSE governing the SC generation in a linearly birefringent fiber can be written as [50, 55],

$$\frac{\partial U_1}{\partial z}-\frac{i\Delta\beta_0 U_2}{2}+\frac{\Delta\beta_1}{2}\frac{\partial U_2}{\partial \tau}-\sum_{k\geq 2}\frac{i^{k+1}\beta_k}{k!}\frac{\partial^k U_1}{\partial \tau^k}= \frac{1}{L_{NL}}\left(i-\frac{1}{\omega_0}\frac{\partial}{\partial \tau}\right)\left(f_R U_1\int_{-\infty}^{\infty}h_R(\tau-\tau')\left[|U_1(\tau')|^2+|U_2(\tau')|^2\right]d\tau'+(1-f_R)U_1\left[\frac{2}{3}|U_1|^2+\frac{4}{3}|U_2|^2\right]\right) \quad (1)$$

$$\frac{\partial U_2}{\partial z}-\frac{i\Delta\beta_0 U_1}{2}+\frac{\Delta\beta_1}{2}\frac{\partial U_1}{\partial \tau}-\sum_{k\geq 2}\frac{i^{k+1}\beta_k}{k!}\frac{\partial^k U_2}{\partial \tau^k}= \frac{1}{L_{NL}}\left(i-\frac{1}{\omega_0}\frac{\partial}{\partial \tau}\right)\left(f_R U_2\int_{-\infty}^{\infty}h_R(\tau-\tau')\left[|U_2(\tau')|^2+|U_1(\tau')|^2\right]d\tau'+(1-f_R)U_2\left[\frac{2}{3}|U_2|^2+\frac{4}{3}|U_1|^2\right]\right) \quad (2)$$

In Eqs. (1) and (2), U_1, U_2 are the envelopes of two circularly polarized eigenstates normalized by the square root of incident peak power (i.e., $\sqrt{P_0}$), and are functions of propagation fiber length z and the retarded time frame τ moving with the pump field. The two linearly polarized eigenstates U_x, U_y along the slow axis (x-axis) and the fast axis (y-axis) of the fiber can be derived from U_1 and U_2 using

$$U_x=\frac{U_1+U_2}{\sqrt{2}}\exp\left(-\frac{i\Delta\beta_0}{2}z\right)$$
$$U_y=\frac{U_1-U_2}{\sqrt{2}}\exp\left(\frac{i\Delta\beta_0}{2}z\right) \quad (3)$$

For an incident pump field ($U_{z=0}$) linearly polarized at an angle θ to the x-axis (slow-axis) of the fiber, the input circularly polarized eigenstates can be expressed as

$$U_1=\frac{U_{z=0}}{\sqrt{2}}\exp(i\theta)$$
$$U_2=\frac{U_{z=0}}{\sqrt{2}}\exp(-i\theta) \quad (4)$$

Also, ω_0 is the central angular frequency of the pump laser, f_R is a constant of 0.18, and L_{NL} is the nonlinear length that can be calculated by $1/(\gamma P_0)$, where γ is the nonlinear coefficient of the fiber. The Raman response function $h_R(t)$ in Eqs. (1) (2) can be written as [57],

$$h_R(t)=\frac{\tau_1^2+\tau_2^2}{\tau_1\tau_2^2}\exp(-\frac{t}{\tau_2})\sin(\frac{t}{\tau_1}) \quad (5)$$

where τ_1 = 12.2 fs and τ_2 = 32 fs. The terms associated with $\Delta\beta_0$ (phase birefringence) and $\Delta\beta_1$ (group delay) reflect the effects of the fiber birefringence on the SC generation. Both $\Delta\beta_0$ and $\Delta\beta_1$ can be measured by dedicated experiments [58–60], and are related to fiber linear birefringence B ($B = n_x$-n_y, i.e., the differential refractive index between two principal axes) by $\Delta\beta_0 = \omega_0 B/c$ (c is the light speed in vacuum) and by $\Delta\beta_1 = \varepsilon B/c$, where ε is a constant varying from 0.38 to 1.3 (at 1550 nm) for the PCFs similar to the DFDD-ANDi PCF [58, 60].

The C-GNLSE-based simulation [Eqs. (1), (2)] retains all parameters required for the corresponding S-GNLSE-based simulation (summarized in Table 2 in [4],), but introduces three additional polarization-related parameters $\Delta\beta_0$, $\Delta\beta_1$, and θ. The calculation largely follows the split-step Fourier method reported previously [4]. We vary $\Delta\beta_0$ within 0.2-80

#156169 - $15.00 USD Received 7 Oct 2011; revised 16 Dec 2011; accepted 17 Dec 2011; published 4 Jan 2012

rad/m, corresponding to a B range of [3.3 × 10^{-8}, 1.3 × 10^{-5}], and $\Delta\beta_1$ within <0.22 ps/m, corresponding to a realistic ε range of [0, 5]. For any given θ, the $\Delta\beta_1$-related term is found out to be negligibly small in comparison to the $\Delta\beta_0$-related term, and can be safely neglected. This simplification is justifiable for weakly birefringent fibers [57], and was invoked in similar situations [50, 55]. To suppress the plausible spontaneous noise amplification in the x-axis and y-axis, the incident polarization angle θ is set at 1° and 89° (rather than 0° and 90°), respectively [55, 56]. The small offset of θ may also reflect the imperfect linear polarization of the incident laser pulses. Thus, the simulation is conducted in a two-dimensional map of [B, θ] [Fig. 4(a)-4(i)]. The results are represented by total spectrum (summed spectral intensities of x-axis and y-axis) and polarization partition ratio p_x, defined as $p_x = P_x/(P_x + P_y)$, where P_x and P_y are the optical intensities in x-axis and y-axis, respectively.

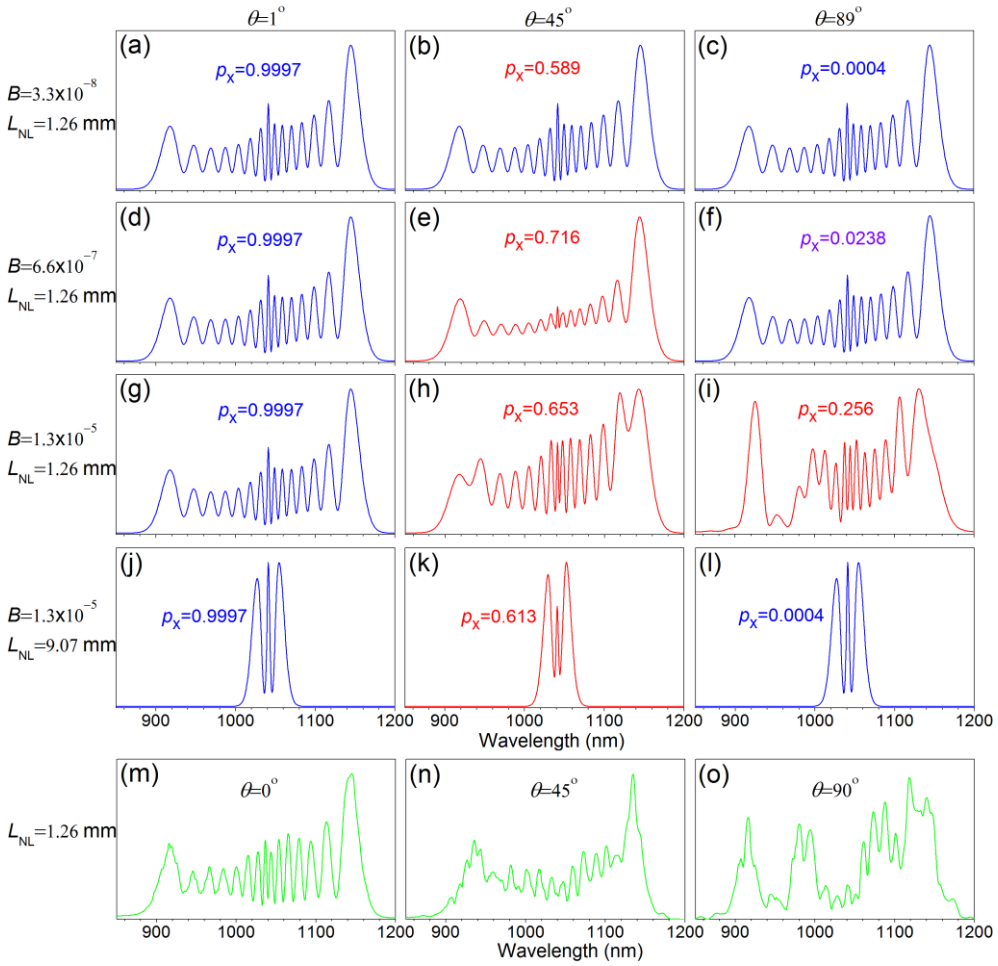

Fig. 4. (a)-(l): Calculated spectrum and polarization partition ratio (p_x) of SC from C-GNLSE at a number of linear birefringence values B, nonlinear length L_{NL}, and incident angles θ. Red labels or curves indicate the significant departures from the S-GNLSE-based simulations on an isotropic fiber. (m)-(o): Observed spectrum of SC at a number of nonlinear length L_{NL}.

At a very weak B of 3.3×10^{-8}, the total spectrum of SC output approximates that shown in Fig. 3(a) and is independent on θ, while the p_x values at θ = 1° and θ = 89° indicate the polarization-maintaining (PM) performance along the two principal axes [Fig. 4(a), 4(c)]. These observations recover the conclusions of the S-GNLSE on a non-birefringent fiber, and thus ensure the correctness of the simulation by the C-GNLSE. However, the p_x value at θ =

#156169 - $15.00 USD Received 7 Oct 2011; revised 16 Dec 2011; accepted 17 Dec 2011; published 4 Jan 2012

45° is attained at 0.589 rather than the expected value of 0.5 from the non-birefringent fiber, indicating the prominent effect of nonlinear polarization rotation. This is a somewhat surprising result considering the small value of the birefringence.

At an elevated B of 6.6×10^{-7}, the onset of cross-phase modulation leads to a significantly modified total spectrum at $\theta = 45°$. This modification to the total spectrum around $\theta = 45°$ results in a 90° rotational symmetry of the total spectrum [Fig. 4(d)-4(f)]. The dependence of the total spectrum on θ is very weak near the slow-axis. Relatively similar results are obtained in a wide θ range of 0° ± 20°. However, this dependence becomes stronger near the fast-axis, as the insensitive range of θ shrinks by 4-fold to 90° ± 5°. This difference between the two principal axes can be attributed to the onset of the vector modulation instability (or polarization modulation instability) in the fast-axis [50, 55, 57, 61].

At the highest B of 1.3×10^{-5}, the total spectrum becomes significantly different from the S-GNLSE-generated spectrum in Fig. 3(a) at $\theta = 89°$, even though they remain in agreement at $\theta = 1°$ [Fig. 4(g), 4(i)]. The dependence of the total spectrum on θ remains weak near the slow-axis, with an insensitive θ range of 0°±20°. However, this dependence becomes extremely sensitive near the fast-axis, and the S-GNLSE-generated spectrum in Fig. 3(a) can only be recovered within 90°±0.0005°, which is practically unobservable. This unusual disparity between the two principal axes exhibits the fully developed vector modulation instability near the fast-axis, breaks the 90° rotational symmetry of the total spectrum at lower B, and results in a reduced rotational symmetry of 180° [Fig. 4(g)-4(i)]. Also, in contrast to the slow-axis pump that generates PM SC [$p_x \approx 1$, Fig. 4(g)], the fast-axis pump produces rather irregular p_x that is highly sensitive to θ [$p_x = 0.256$, Fig. 4(i)].

To summarize, the SC generation in the DFDD-ANDi PCF is profoundly affected by the weak birefringence of the fiber, and must be modeled according to the C-GNLSE. The easily observable qualitative difference of some θ-dependent polarization effects can be used to semi-quantitatively estimate the magnitude of this birefringence.

3.3 Remarks on situations where S-GNLSE is highly successful

The results in Fig. 4(a)-4(i) contrast sharply to the established studies in which the S-GNLSE was highly successful to interpret, for example, soliton self-frequency shift/dispersive wave generation [62], soliton self-frequency shift cancelation [63], spectrogram evolution [64, 65], relative intensity noise [66], and optical rogue waves [67]. None of these unusual physical phenomena require the more complicated interpretation by the C-GNLSE. It should be noted that all these studies were performed on ZDW PCFs to generate solitons, and the nonlinear polarization properties of the solitons could be quite different from those of the pulses propagating in the DFDD-ANDi PCF [68]. However, here we highlight the effect of nonlinear length L_{NL} ($1/\gamma P_0$), which represents the combined nonlinearity of small fiber core (γ) and incident peak intensity (P_0). The results in Fig. 4(a)-4(i) are obtained at $L_{NL} = 1.26$ mm. This length is at least 7 times shorter than the above studies on the ZDW PCFs, i.e., we study the SC generation at a regime of much stronger nonlinearity. If L_{NL} is lengthened to 9.07 mm by lowing P_0, the nonlinear polarization effects at $B = 1.3 \times 10^{-5}$ become less pronounced [Fig. 4(j)-4(l)]. We even verify the absence of these effects in the fast-axis in long (~1 m) pieces of the DFDD-ANDi PCF. Thus, the weaker nonlinearity may be the single most important factor to diminish the nonlinear polarization effects (i.e., to validate the S-GNLSE) in those studies.

4. Experiments and discussion

4.1 Experimental evidence supporting the predicted polarization effects

Our experimental setup was described in detail previously [4], so only a brief summary is given here. A solid-state Yb:KYW laser (FemtoTRAIN, High-Q laser GmbH, Austria) was used to pump a 9-cm long DFDD-ANDi PCF (NL-1050-NEG-1, NKT Photonics, Denmark) with linearly polarized 1041-nm 229-fs 76-MHz pulses (Fig. 5). The polarization angle of the incident laser pulses was varied by a half wave-plate with 0.2° rotation accuracy, and the pulses after the wave-plate had a measured polarization extinction ratio (PER) of >25 dB. An

#156169 - $15.00 USD Received 7 Oct 2011; revised 16 Dec 2011; accepted 17 Dec 2011; published 4 Jan 2012

aspheric lens provided a free-space-to-fiber light coupling of ~55% efficiency. The average power of the SC exiting the fiber (fiber transmission power) was typically 0.36 W, but was occasionally lowered (by the attenuator) to 0.05 W to eliminate certain nonlinear optical effects. An optical spectrum analyzer was used to record the total spectrum of the SC collimated by another aspheric lens. A broadband polarizer and a power meter were used to measure the polarization partition ratio p_x of the SC.

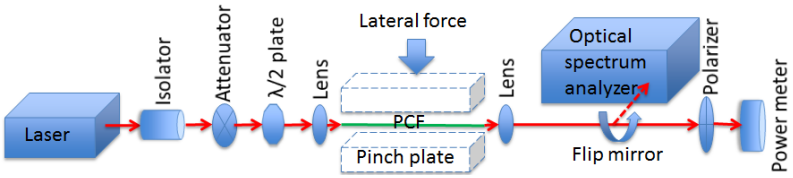

Fig. 5. Schematic of PCF SC generation and corresponding measurements of total spectrum and polarization properties. Two pinch plates may be used to stress the PCF through lateral force.

The generation of the 0.36 W SC produced the S-GNLSE-quantified spectrum [Fig. 3(a)] when the incident polarization angle θ was set close to one of the principal axis of the fiber [4]. The total spectrum at other θ was noticeably different from the S-GNLSE-quantified spectrum. This excludes the possibility that B is as small as 3.3×10^{-8}. Also, by identifying the rotation symmetry of the total spectrum with respect to the S-GNLSE-quantified spectrum, a rotational symmetry of 180° (not 90°) was observed. Thus, B cannot be as small as 6.6×10^{-7}. Finally, two orthogonal axes of the fiber with dramatically different sensitivity of SC generation to θ were identified. In one axis, the S-GNLSE-quantified spectrum was attained with very weak sensitivity to θ (±10°). In the other axis, however, a dramatically different total spectrum was generated, and the exact profile of the spectrum was sensitive to a small perturbation (±1°) of θ. The total spectrum generated at an intermediate θ between the two axes was also different from the S-GNLSE-quantified spectrum. This evidence is highly consistent with the prediction from the C-GNLSE [Fig. 4(g)-4(i)], indicating that B is on the order of 1.3×10^{-5}, and allowing unambiguous identification of the slow-axis and the fast-axis. The examination of the rotational symmetry of the SC generation is a simple experiment widely used to evaluate the underlying polarization effects. However, previously observed ~60° [50, 51] and 40°-60° (or 180°) [52] rotational symmetry have not been used to semi-quantitatively estimate B.

Once the slow-axis of the fiber was identified, the SC spectra were recorded at $\theta = 0°$ [Fig. 4(m)], $\theta = 45°$ [Fig. 4(n)], and $\theta = 90°$ [Fig. 4(o)]. Qualitative agreement is found between the observed spectra and the simulated spectra corresponding to $B = 1.3 \times 10^{-5}$ [Fig. 4(g), 4(h), 4(i)].

A cutback method was used to independently confirm the estimated B. The Yb:KYW laser was operated in CW mode, and the emitted linearly polarized (>25 dB PER) CW light was coupled into a straightly mounted ~25 cm long fiber. The coupling efficiency was ~60% at a constant incident CW power of ~0.3 W, and was independent of the rotation of the half wave plate. Two orthogonal incident angles were identified for the half wave-plate to maximize the PER of the fiber output at 15-20 dB along two optimized orthogonal orientations of the polarizer [Fig. 5, Fig. 6(a)]. Thus, the fiber has two principal axes along which linearly polarized input CW light (>25 dB PER) largely retains its linear polarization (15-20 dB PER), i.e., the fiber can be loosely treated as a linearly birefringent fiber. However, the detectable 5-10 dB depolarization suggests the superimposition of a weaker circular birefringence on B. Consistently, the orientations of the two orthogonal principal axes at the entrance facet of the fiber (identified by the half wave-plate) and the exit facet of the fiber (identified by the polarizer) have a measurable 5 ± 2° "twist" along the ~25-cm fiber length.

#156169 - $15.00 USD Received 7 Oct 2011; revised 16 Dec 2011; accepted 17 Dec 2011; published 4 Jan 2012

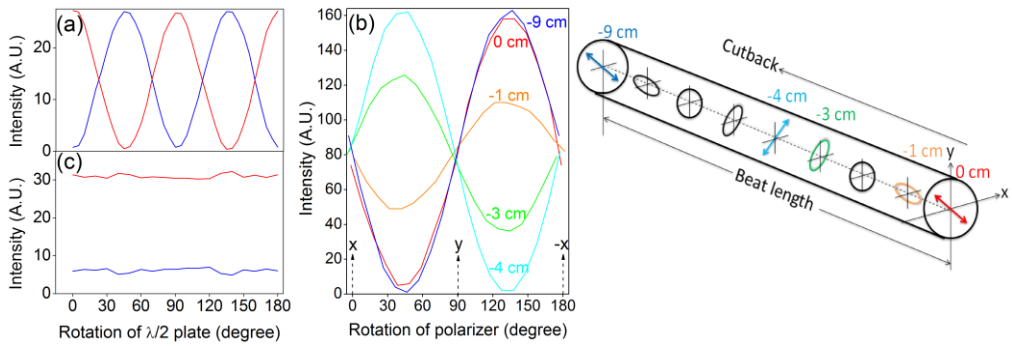

Fig. 6. (a) Intensity of 1041-nm CW light as a function of half wave-plate rotation when the polarizer is set along one of the two principal axes of the fiber (red or blue curve); (b) Left: intensity of 1041-nm CW light as a function of polarizer rotation at several cutback lengths when the incident polarization is set at 45° to the *x*-axis; Right: diagram shows the corresponding evolution of the polarization state in the fiber; (c) Intensity of 0.36 W SC as a function of half wave-plate rotation when the polarizer is set along one of the two principal axes of the fiber (red or blue curve).

With the two principal axes identified at both the entrance and the exit facets of the fiber, the polarization of the incident CW beam was oriented at 45° between the two axes, and fiber cutback was conducted at 1.0 cm intervals to measure the periodicity of the polarization state of the fiber output, i.e., the beat length [Fig. 6(b)]. The measured beat length was 9 cm [Fig. 6(b)], with ±3.0 cm variation among different testing fibers. This beat length corresponds to $B = 1.3 \pm 0.6 \times 10^{-5}$ at 1041-nm, which agrees well with the estimated B by the C-GNLSE. One advantage of the cutback measurement is the ability to probe the uniformity of B across a short fiber. Figure 6(b) shows that it may take either a 4-cm cut or a 5-cm cut to flip the linear polarization state to its orthogonal orientation, i.e., B in this 9-cm long fiber has a local variation of 20%. This randomness suggests the unintentional nature of B.

It is rather surprising that a relatively large (1×10^{-5}) B emerges from the highly symmetric cross-section of the PCF [Fig. 3(b), inset]. We note that the core diameter of the PCF was only 2.3 μm, which is much smaller than that of large-mode-area PCFs or conventional telecommunication fibers. Thus, this magnitude of B may be inherent to the fabrication of the nonlinear (small-core) optical fibers in which unintentional structural symmetry breaks of the fiber are prevalent. Independent measurements by NKT Photonics (major supplier of commercial PCFs) confirm that the nonlinear PCFs with a highly symmetric cross-section and a comparable core size (including many popular ZDW PCFs) feature a B on the level of 10^{-5}, even though these fibers are not intended for PM applications.

4.2 Observation and interpretation of "constant" elliptical state in longer fibers

We have shown the benefits of the C-GNLSE over the S-GNLSE in understanding the rotational symmetry/sensitivity of the SC generation in the short (9-cm) PCF. Here we demonstrate how the C-GNLSE is necessary to interpret an "intriguing" nonlinear polarization effect in longer pieces (80-200 cm) of this PCF. The coupling efficiency of the pump pulses in these fibers was also ~55% (i.e., the loss in the PCFs can be neglected) so that 0.36 W SC was produced just like in the case of the short fiber, but with a much broader spectrum [48]. Unexpectedly, the SC was in a "constant" elliptical state with a measured PER of 7 dB [Fig. 6(c)]. If the polarizer was oriented along the long-axis (or short-axis) of the elliptical state, the output power after the polarizer was (nearly) independent on the incident polarization [Fig. 6(c)]. Interestingly, the elliptical state was not sensitive to regular fiber bending, and was preserved in wide ranges of fiber lengths (80-200 cm) and fiber transmission power (>0.33 W). In a S-GNLSE-based interpretation, one would intuitively expect the rotation of the elliptical state with the incident polarization.

#156169 - $15.00 USD Received 7 Oct 2011; revised 16 Dec 2011; accepted 17 Dec 2011; published 4 Jan 2012

The elliptical state completely disappeared when the fiber transmission power was lowered to 0.05 W. At this power, the dependence of the output power after the polarizer on the incident polarization recovered the sinusoidal profiles of linear fiber optics [Fig. 6(a)], if the polarizer was set along the long-axis or short-axis of the elliptical state. This procedure indicates that the "constant" elliptical state is a nonlinear polarization effect, and the long- and short-axes of the elliptical state correspond to the two principal axes of the fiber at the exit facet. However, it is unclear whether the long-axis of the elliptical state corresponds to the slow-axis or fast-axis of the fiber. To determine this, a cutback experiment was performed on a straight-mounted fiber from a length of 85 cm to 9 cm. For each length, the principal axes of the fiber at both the entrance and the exit facets were first identified at the low fiber transmission power (0.05 W) by retrieving the sinusoidal profiles of Fig. 6(a). Then, both the incident polarization and the output polarization were set along one of the principal axes of the fiber to examine the depolarization of the incident pulses along this axis. The depolarization is defined as $P_{\perp}/(P_{\parallel} + P_{\perp})$, where $P_{\parallel}$ is the power remaining in the principal axis along which the incident pulses are injected, and $P_{\perp}$ is the incident power coupled into the other principal axis. Finally, the measured depolarization as a function of fiber length was plotted for the two principal axes at low or high fiber transmission power (0.05 W or 0.36 W) [Fig. 7(a), 7(b)].

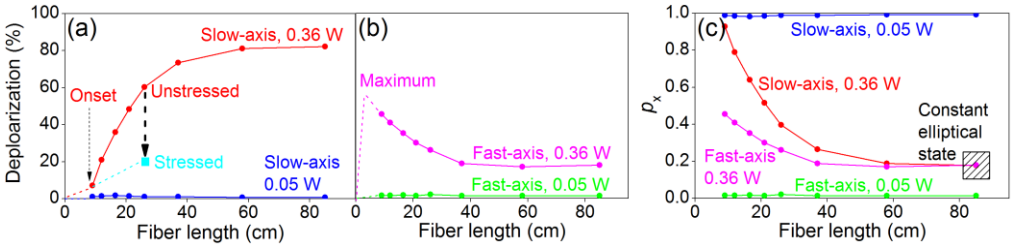

Fig. 7. (a) Dependence of slow-axis depolarization on fiber length, average fiber transmission power, and lateral stress; (b) Dependence of fast-axis depolarization on fiber length and average fiber transmission power; (c) Dependence of polarization partition ratio p_x in two principal axes on fiber length and average fiber transmission power. At 0.36 W, the p_x values in two axes reach a constant in long (>80 cm) fibers.

At the low fiber transmission power of 0.05 W (corresponding to L_{NL} = 9.07 mm), the pulses in either axis encounter negligible depolarization [Fig. 7(a), 7(b)]. This observation is consistent with the conclusions from the C-GNLSE. At the high fiber transmission power of 0.36 W (L_{NL} = 1.26 mm), however, the pulses in the two axes encounter dramatically different depolarization at various propagating lengths. At 9-cm propagating length, the pulses in one axis encounter a small depolarization (7%) [Fig. 7(a)] to attain a total spectrum and p_x (0.93) that approximate those of Fig. 4(g), while the pulses in the other axis suffer a large depolarization (46%) [Fig. 7(b)] to attain a total spectrum and p_x (0.46) that resemble those of Fig. 4(i). Thus, the C-GNLSE-based simulation and the cutback experiment allow unambiguous assignment of the slow-axis (or fast axis) to the principal axis associated with Fig. 7(a) [or Fig. 7(b)]. One could mistakenly assign the fast-axis to the slow axis because it appears to be more polarization-preserving in longer fiber lengths [Fig. 7(a), 7(b)].

The 0.36 W pulses in the slow-axis continuously depolarize with increasing propagating length, while those in the fast-axis go through a maximum depolarization in the first 9-cm of the propagating length but partially recover the polarization in longer propagating lengths. The depolarization profiles of Fig. 7(a), 7(b) can be transformed to the p_x profiles in Fig. 7(c), which clearly shows how the same elliptical state is attained for either a slow-axis pump or a fast-axis pump. The elliptical state stays "constant" in longer fiber lengths (>80 cm) because of the diminished nonlinear optical effect, corresponding to the limited spectral broadening and lengthened pulse temporal spreading.

It should be noted that the C-GNLSE-simulated SC generation at 0.36 W transmission power forbids any depolarization effect in the slow-axis, which is considerably different from

#156169 - $15.00 USD Received 7 Oct 2011; revised 16 Dec 2011; accepted 17 Dec 2011; published 4 Jan 2012

the observed profile [Fig. 7(a)]. This discrepancy can be easily attributed to the presence of a small circular birefringence (10^{-8}-10^{-6}), just like the presence of small B redistributes the powers in the two principal axes through nonlinear polarization rotation [Fig. 4(b)] or cross-phase modulation [Fig. 4(e)]. We believe the complete understanding of the "constant" elliptical state can be resort to the more complicated C-GNLSE that takes into account both the linear and circular birefringence. Specific experiments have been designed to measure the circular birefringence of the PCFs on the order of 10^{-4}-10^{-3} [69, 70], but these are questionable methods to measure the weak circular birefringence of this DFDD-ANDi PCF of plausible random nature.

4.3 Remarks on pulse compression

Rigorous modeling of the SC generation in long (>9 cm) pieces of the weakly birefringent DFDD-ANDi PCF for pulse compression along the third path [Fig. 2(c)] requires accurate knowledge of the (linear and circular) birefringence of fiber, which may be difficult to measure. The SC generation of these fibers is extremely sensitive to the value of the weak birefringence through vector nonlinear processes of nonlinear polarization rotation, cross-phase modulation, and polarization modulation instability. The C-GNLSE-based simulation shows that the resulting SC pulses may have temporally split profiles and unsmooth spectral phases that dramatically modify those predicted from the S-GNLSE (Fig. 3). These modifications are undesirable for high-quality pulse compression. Also, the local random variation of the linear and circular birefringence may further complicate the rigorous theoretical modeling to guide the pulse compression, and may be responsible for the discrepancy between the observed SC spectra [Fig. 4(n), 4(o)] and the simulated spectra [Fig. 4(h), 4(i)] . These observations make it difficult, if not impossible, to implement high-compression-ratio (>24) pulse compression of SC from these fibers along the third path.

5. Toward a practical coherent fiber supercontinuum laser

5.1 Simulation of SC generation in a polarization-maintaining DFDD-ANDi PCF

The simulation by the C-GNLSE indicates that the SC generation from the PCF is insensitive to the exact value of B and the small perturbation of the incident polarization if the incident polarization is oriented along the slow-axis of the fiber [Fig. 4(a), 4(d), 4(g)]. Thus, the above difficulty of pulse compression due to weak unintentional birefringence may be avoided by introducing a strong intentional linear (form- or stress-) birefringence to suppress the unintentional birefringence [Fig. 8(a)], and aligning the incident polarization along the slow-axis of this strongly birefringent fiber.

To explore this possibility, we assume that the same DFDD-ANDi PCF can be fabricated except that two stress rods are applied to the cladding of the fiber [Fig. 8(a), bottom left]. This design introduces a large B without affecting the dispersion of the fiber. Assuming $B = 10^{-4}$, $\Delta\beta_1 < 5B/c$, $\theta = 1°$, and a fiber length of 27 cm, we simulate the spectrotemporal field of the SC pulses by the C-GNLSE according to the known parameters (Table 2 in [4],). The output SC has a PM capability ($p_x \approx 1$), and a typical wave-breaking temporal profile indicative of high coherence [Fig. 8(b)] [71], and a smooth spectral phase of mainly linear chirp [Fig. 8(c)], permitting transform-limited pulse compression to 5.5 fs along the third path [Fig. 2(c)]. Our simulation also shows that shorter, unchirped, Gaussian-shaped incident pulses lead to broader SC generation (or shorter pulse compression) and a smoother spectrum.

It should be noted that the results of Figs. 8(b) and 8(c) are insensitive to the exact values of B (~10^{-4}), $\Delta\beta_1$, and θ (within [-1°, 1°]), and can be reduced to the conclusions of the S-GNLSE in this particular case. One could argue that the S-GNLSE of an isotropic fiber might also be applicable to the principal-axis SC generation in a strongly birefringent fiber. This statement is generally incorrect because the S-GNLSE does not specify the sensitivity of the SC generation to θ at a specific B, $\Delta\beta_1$, and fiber dispersion profile. An extremely high sensitivity may unavoidably lead to pulse depolarization (e.g., through polarization modulation instability [72] or cross-phase modulation) and invalidate the principal-axis PM

#156169 - $15.00 USD Received 7 Oct 2011; revised 16 Dec 2011; accepted 17 Dec 2011; published 4 Jan 2012

capability predicted from the S-GNLSE. To date, the principal-axis PM capability of strongly birefringent fibers has only been justified by the C-GNLSE [73] or experimentally validated [73–75] in a rather low nonlinearity (L_{NL}>5 mm) regime of SC generation.

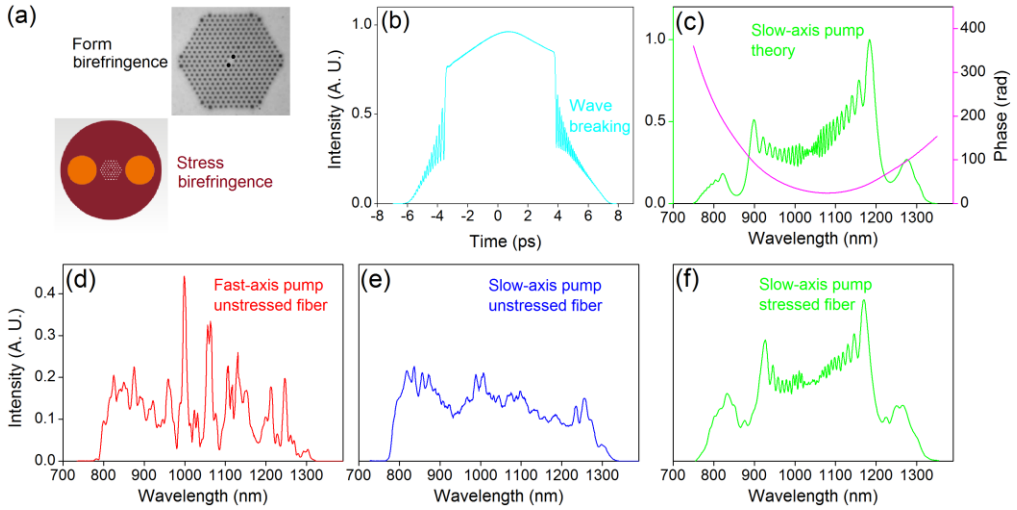

Fig. 8. (a) Two representative designs of PM PCFs; (b) Calculated temporal profile of the SC from a 27-cm PM DFDD-ANDi PCF with a slow-axis pump; (c) Calculated spectrum and spectral phase of the SC from a 27-cm PM DFDD-ANDi PCF with a slow-axis pump; (d) Observed spectrum of a unstressed 27-cm DFDD-ANDi PCF with a fast-axis pump; (e) Observed spectrum of a unstressed 27-cm DFDD-ANDi PCF with a slow-axis pump; (f) Observed spectrum of a stressed 27-cm DFDD-ANDi PCF with a slow-axis pump.

5.2 Suppression of nonlinear polarization effects by lateral stress

For simplicity, the above simulation on the PM DFDD-ANDi PCF ignores any circular birefringence. A natural question arises whether a weak circular birefringence can depolarize the SC generated in the slow-axis along the 27-cm fiber length, as in the case of the weakly birefringent PCF [Fig. 7(a)]. We believe that this circular-birefringence-induced depolarization can be minimized by increasing the ratio of B over the circular birefringence, i.e., decreasing the ellipticity of the birefringence. This assumption can be tested by externally stressing the available weakly birefringent PCF.

The slow-axis of a 27-cm bare fiber piece of this PCF was first identified, and then oriented along the horizontal direction. The total spectra of the 0.36 W SC output with a fast-axis pump and a slow-axis pump are shown in Fig. 8(d) and Fig. 8(e), respectively. The former has a structured profile, which is likely due to the pulse interference caused by the depolarization maximum [Fig. 7(b)]. The later bears little resemblance to the simulated spectrum [Fig. 8(c)]. This is not unexpected considering the significant depolarization at a 27-cm fiber length [Fig. 7(a)]. A pair of 26-cm long stainless steel pinch plates was then applied to the PCF to introduce a vertical lateral force of 200 N [Fig. 5], corresponding to an induced B of ~4×10^{-5} [76]. The superimposition of this B on the unintentional birefringence (1.3×10^{-5}) should significantly decrease the ellipticity of the birefringence. Under the lateral stress, the total spectrum with the slow-axis pump [Fig. 8(f)] was in good agreement with the simulated spectrum, while the depolarization of the SC was decreased from 60% to 21% [Fig. 7(a)]. We believe that the residual depolarization and other circular-birefringence-related nonlinear polarization effects can be completely suppressed in the PM DFDD-ANDi PCF having a large built-in B (~1×10^{-4}).

The proposed PM DFDD-ANDi PCF is a promising candidate to develop a practical coherent fiber SC laser with a highly polarized output. The spectrotemporal field of the SC induced by a slow-axis pump can be reliably predicted without accurate knowledge of B, $\Delta\beta_1$,

#156169 - $15.00 USD Received 7 Oct 2011; revised 16 Dec 2011; accepted 17 Dec 2011; published 4 Jan 2012

and the ellipticity of the fiber, and without precise control (<1°) of θ or critical demand of incident polarization linearity (>30 dB PER). The smooth spectral phase of SC pulses [Fig. 8(c)] permits simple transform-limited pulse compression along the third path [Fig. 2(c)].

6. Conclusions

The C-GNLSE successfully explains the observed rotation symmetry/sensitivity of the SC generation and the principal-axis pulse depolarization in a short (9-cm) non-PM DFDD-ANDi PCF. More importantly, the C-GNLSE unambiguously identifies the uncontrolled intrinsic birefringence as the main factor that limits the accuracy of the S-GNLSE to model the SC generation in long (>9 cm) pieces of this PCF, and their application in broadband SC pulse compression. The polarization evolution of longer fibers (80-200 cm) can lead to a "constant" elliptical state independent of incident polarization and propagation length, which we attribute to the circular-birefringence-related nonlinear effects accumulated along the fiber. To avoid the deleterious effects of this birefringence on predictable SC generation, the C-GNLSE-based simulation and a specially designed experiment have guided the design of a PM DFDD-ANDi PCF that could be useful to develop a practical coherent fiber SC laser. The theoretically-quantified SC output of this laser allows high-compression-ratio (>24) transform-limited pulse compression.

Acknowledgments

We thank Dr. Peter Dragic and Darold Spillman for their technical and logistical contributions to this project, and High-Q Laser GmbH and NKT Photonics for their generous offers of pump lasers and PCFs. This work was supported by grants from the National Institutes of Health (NCI R21/R33 CA115536; NIBIB R01 EB012479; NCI RC1 CA147096, S.A.B.), and from the Danish Council for Independent Research—Technology and Production Sciences (FTP). Additional information can be found at http://biophotonics.illinois.edu.

#156169 - $15.00 USD Received 7 Oct 2011; revised 16 Dec 2011; accepted 17 Dec 2011; published 4 Jan 2012